





Structural diversity of Alzheimer-related protein aggregations revealed using photothermal ratio-metric micro-spectroscopy

SIMING WANG,¹ WENHAO ZHANG,² PENGCHENG FU,¹ YAN ZHONG,^{3,4} KIRYL D. PIATKEVICH,^{2,8} DELONG ZHANG,^{1,5,6,9}  AND HYEON JEONG LEE^{5,7,10} 

¹Zhejiang Key Laboratory of Micro-nano Quantum Chips and Quantum Control, and School of Physics, Zhejiang University, Hangzhou 310027, China

²School of Life Sciences, Westlake University, Westlake Laboratory of Life Sciences and Biomedicine, Institute of Basic Medical Sciences, Westlake Institute for Advanced Study, Hangzhou 310024, China

³Department of Nuclear Medicine and PET Center, The Second Affiliated Hospital of Zhejiang University School of Medicine, Hangzhou 310024, China

⁴Institute of Nuclear Medicine and Molecular Imaging, Zhejiang University, Hangzhou 310024, China

⁵MOE Frontier Science Center for Brain Science & Brain-Machine Integration of Zhejiang University, Hangzhou 310027, China

⁶Innovative and Entrepreneur Team of Zhejiang for Year 2020 Biomarker Driven Basic and Translational Research on Major Brain Diseases, Zhejiang University, Hangzhou 310027, China

⁷College of Biomedical Engineering & Instrument Science, Key Laboratory for Biomedical Engineering of Ministry of Education, Zhejiang University, Hangzhou 310027, China

⁸kiryl.piatkevich@westlake.edu.cn

⁹dlzhang@zju.edu.cn

¹⁰hjlee@zju.edu.cn

Abstract: The crucial link between pathological protein aggregations and lipids in Alzheimer's disease pathogenesis is increasingly recognized, yet its spatial dynamics remain challenging for labeling-based microscopy. Here, we demonstrate photothermal ratio-metric infrared spectro-microscopy (PRISM) to investigate the *in situ* structural and molecular compositions of pathological features in brain tissues at submicron resolution. By identifying the vibrational spectroscopic signatures of protein secondary structures and lipids, PRISM tracks the structural dynamics of pathological proteins, including amyloid and hyperphosphorylated Tau (pTau). Amyloid-associated lipid features in major brain regions were observed, notably the enrichment of lipid-dissociated plaques in the hippocampus. Spectroscopic profiling of pTau revealed significant heterogeneity in phosphorylation levels and a distinct lipid-pTau relationship that contrasts with the anticipated lipid-plaque correlation. Beyond *in vitro* studies, our findings provide direct visualization evidence of aggregate-lipid interactions across the brain, offering new insights into mechanistic and therapeutic research of neurodegenerative diseases.

© 2024 Optica Publishing Group under the terms of the [Optica Open Access Publishing Agreement](#)

1. Introduction

Protein structure abnormalities are implicated in various diseases, often characterized by protein aggregations, including β -sheet-rich aggregates [1,2], oligomers [3], plaques, and neurofibrillary tangles (NFTs) [4], frequently serve as molecular markers in neurodegenerative diseases [5,6]. The identification and characterization of disease-specific protein conformations and intermolecular interactions are crucial for developing diagnostic and therapeutic strategies, especially in prevalent neurodegenerative diseases such as Alzheimer's disease (AD). However, developing treatments based on these pathological protein structures has been challenging due to an incomplete understanding of how these pathological proteins develop or interact with their surrounding

structures or molecules [7,8]. Recent findings highlight the pathophysiological heterogeneity of AD, which results in subtypes of diseases with different clinical symptoms and responses to treatments [9], urging a deeper understanding of the structural diversity of these pathological proteins.

AD is characterized by the extracellular deposition of amyloid- β (A β) plaques and intracellular aggregation of hyperphosphorylated Tau (pTau) in the form of NFTs. These protein structures exhibit specific conformations rather than random aggregates [10,11]. Importantly, amyloid polymorphism was observed and studied [12,13], indicating the existing heterogeneity in the protein structures. However, the mechanism underlying these heterogeneities in disease progression remains elusive because it is difficult to label polymorphic proteins with antibodies. Meanwhile, although lipid accumulation was one of the earliest pathological observations in AD [14], it has been relatively less studied due to difficulties in visualizing these molecules. Nonetheless, recent progress in elucidating the link between protein aggregation and lipids [15–18] highlights the importance of simultaneously detecting protein structures and lipid contents to provide molecular insights into AD pathogenesis.

Molecular vibrational spectroscopy has emerged as a promising method for detecting disease-specific molecular markers. Raman spectroscopy [19] and coherent Raman scattering imaging [20,21] have been employed in AD detection by locating plaques through the β -sheet Raman band at 1670 cm^{-1} . However, SRS imaging in the fingerprint region usually suffers from low signal levels, presenting challenges in further differentiating the arrangement of secondary structures such as parallel and antiparallel β -sheets [22]. Alternatively, infrared (IR) spectroscopy also originates from molecular vibration with orders of magnitude higher signal levels. Specifically, IR spectroscopy, focusing on the amide I band [23,24], has been widely utilized for studying protein secondary structures with large absorption cross-sections in bulk measurement. Fourier-transform infrared spectroscopy [25] and imaging [26] have been employed to study amyloid plaques in AD, revealing changes in protein β -sheet levels during plaque formation and increased lipid oxidation in AD patients with micron resolution [27]. Discrete-frequency infrared imaging, using a quantum cascade laser, has identified distinct plaque morphologies [28]. However, the limited spatial resolution due to the optical diffraction limit makes it challenging to resolve spatial profiles of protein structural diversity and their intricate interaction with other biomolecules, which is below the micron in distance. Alternatively, the atomic force microscopy-IR technique provides substantially higher spatial resolution [29,30] but is difficult to implement in tissue samples with high throughput for whole-brain slice imaging.

The recent development of mid-infrared photothermal (MIP, also known as O-PTIR) imaging addresses these challenges through a pump-probe detection scheme, providing submicron spatial resolution, minimal spectral artifacts, and compatibility with aqueous samples [31–33] in molecular-selective imaging of living cells, tissue slices, and organisms [34–40]. In neurology studies, MIP has demonstrated the visualization of traveling protein vesicles in live neurons [35], the spectral features of β -sheet aggregation and isolated fibrils in dendrites and spines [41], and fluorescence-guided 3D imaging of tau fibrils in a single cell [42]. However, cellular studies have limited clinical relevance, urging for tissue-level investigation under physiological conditions. Compared with cell samples, MIP imaging of tissues is significantly more challenging due to the high inhomogeneity of brain tissue, which renders the conventional ratio imaging, i.e., dividing images taken at two wavenumbers, less reliable for identifying plaques. Despite the challenges, MIP tissue studies was realized by the assist of fluorescence to measure the spectrum of plaques in tissues. Prater et al. mapped fluorescently labeled amyloid plaques and acquired IR spectra by fluorescence-guided MIP imaging [43]. However, the labeling-guided approach requires prior knowledge of protein structures and often overlooks information on protein polymorphisms, which have recently become the focus of studying AD pathogenesis.

Here, we report a photothermal ratio-metric infrared spectro-microscopy (PRISM) to extract protein secondary structures based on their spectral features to visualize the pathological protein aggregations. Through the ratio-metric process, PRISM minimizes potential artifacts from variations in nuclear or cellular densities across the brain tissue. Therefore, PRISM quantitatively decomposes the secondary structural compositions of A β plaques and NFT in AD mouse models, revealing the dynamic pathways of how normal proteins and lipids evolve into amyloid- and pTau-lipid interact units. Through MIP spectro-microscopy, amyloid, pTau, and lipids were quantified and analyzed, indicating that the amyloid-lipid interaction in the hippocampal is significantly elevated during the development of AD, and the lipid stability in brain regions associated with motor function is surprising. In addition, we evaluated the relative proportions of different protein conformations during Tau phosphorylation and their evolution rule. The conformation compositions of A β and NFTs and their interactions with lipids provide predictive projections of AD progression, offering insights into metabolic alterations during disease progression. Importantly, PRISM fills a gap in the bio-integration testing of label-free microscopy [44], providing inspiration for cross-scale structural-sensitive bioimaging.

2. Results

Protein aggregates exhibit polymorphism containing varying proportions of protein conformations. Our study focused on the two major protein lesions associated with AD, amyloid and tangles, which follow independent and specific dynamic changes accompanied by lipid interactions (Fig. 1(a)). The spectroscopic imaging is implemented on a MIP microscope, in which mid-infrared nanosecond and continuous green lasers are combined and focused on the sample with an epi-detected photodiode (Fig. 1(b), see Methods for details). The selective vibrational absorption of molecules undergoes vibration relaxation (Fig. 1(c)), resulting in a local temperature increase and a subsequent photothermal relaxation (Fig. 1(d)). This local refractive index modulation leads to a modulation of probe light intensity. The spatial resolution is determined by the probe beam (532 nm), achieving a 387 nm lateral resolution (Fig. S1).

2.1. Identifying the spectroscopic signature of amyloid plaques

To identify the spectroscopic feature of amyloid plaque, we focus on the amide I band (1600–1720 cm^{-1}), a distinctive band of proteins mainly generated by C=O vibration and widely used for imaging biological systems [35,45,46]. We adopted amyloid protein A β 42, a robust AD model, and acquired *in vitro* MIP spectra, which show a distinctive peak at 1633 cm^{-1} (Fig. 1(e)). Although this peak has been attributed to the β -sheet structure [47], such a prominent peak in the amide I band is not commonly observed in actual pathological conditions [28]. In contrast, wildtype (WT) mouse brain, as a reference for normal protein structure in non-pathological tissues, exhibits a different spectral profile peaking at 1655 cm^{-1} (Fig. 1(f)). To further quantify the structural composition, we performed multi-peak deconvolution (see Methods for details). The amyloid is found to have 45% of the total peak area contributed by the β -sheet structure, while WT is measured to have 77% of the area contribution by the α -structure. Therefore, the two key wavenumbers, 1633 and 1655 cm^{-1} , are identified for amyloid and normal tissue, respectively. Nonetheless, the residual components are attributed to turn-like structure (1670 cm^{-1}) and β -sheets (1682 and 1696 cm^{-1}) for amyloid, and β structure (1626 cm^{-1}) and turn-like (1676 cm^{-1}) for WT [48].

To test whether these features could highlight amyloid plaques in complex tissue, whole brain slices from AD mice were imaged by MIP microscopy in the amide I region (Fig. 2(a)). By applying the PRISM process (see Methods for details), an over 4-fold improvement in plaque contrast is shown (Fig. S2). As a result, PRISM images unveiled clear and specific accumulations of β -sheet-enriched proteins in the AD brain (Fig. S3a, d). Meanwhile, such features are not

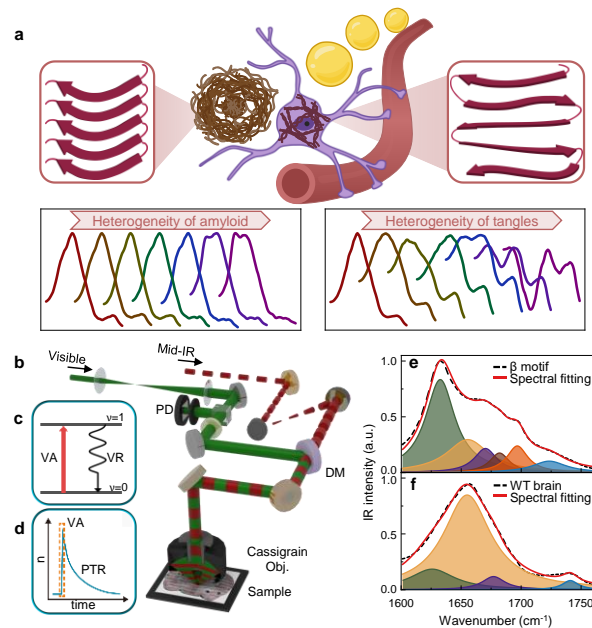


Fig. 1. The concept and implementation of detecting spectroscopic features of abnormal protein aggregations. (a) Spectroscopic tracking of amyloid and tangles. (b) Optical setup of MIP microscope. DM: dichroic mirror. PD: photodiode. (c) Energy diagram of vibrational absorption (VA) and vibrational relaxation (VR). (d) Local temperature increase (dashed box) and photothermal relaxation (PTR). Spectra and analysis of (e) A β 42 and (f) WT brain (collected from 10 locations).

discernible in individual IR images (Fig. S3g-l). The identified plaques exhibited a diameter of $15 \pm 5 \mu\text{m}$ (mean \pm error bound), consistent with previously reported plaque sizes [49].

We first verified the fidelity of PRISM to amyloid. Immunofluorescence (IF) staining targeting A β peptides on the same brain slices confirmed these protein aggregations as pathological amyloid plaques (Fig. S4). The co-localization of the protein aggregations identified by PRISM with stained A β (Fig. S5) demonstrates the reliability of PRISM imaging results. Furthermore, the absence of these protein aggregates in the WT brain (Fig. S3b, e) indicates their specificity to AD.

2.2. Validating plaque pathological levels by protein-lipid profiling

To fully understand the spatial-spectral diversity of these plaques, we performed lipid imaging of the same field of view by tuning to the 1741cm^{-1} peak attributed to the C=O stretching mode. Morphologically, plaques were classified into three types: diffuse, compact, and cored [26,50]. Interestingly, lipid and PRISM imaging revealed that lipid accumulation occurs near some, but not all, of the plaques (Fig. S3c, f). PRISM imaging of β -sheet structure clearly identified three plaque types (Fig. 2(b)-(e)), which was further validated by IF staining (Fig. 2(f)-(i)).

Among them, cored plaques showed unique spatial features of dense A β nucleus at the center surrounded by a lipid-rich halo, potentially linked to the apoptosis of peripheral nerve cells and astrocytes [20,51,52]. Notably, the lipid content within the plaque exhibited a decrease with plaque maturation (Fig. 2(j)-(m)). Quantitative analysis showed a steady increase in the β -sheet level as plaques developed from diffuse to cored (Fig. 2(n)). In contrast, the lipid level gradually decreased (Fig. 2(o)), showing a negative correlation (Pearson correlation coefficient = -0.74)

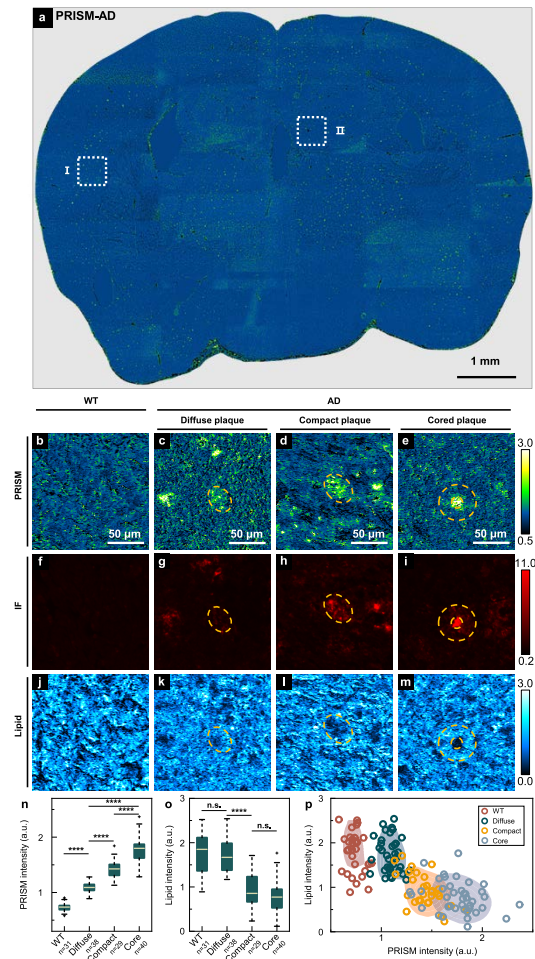


Fig. 2. Visualization of three subtypes of plaques. (a) PRISM map of an AD brain slice, stitched by 50 large-area images of about $1.8 \text{ mm} \times 0.6 \text{ mm}$ each. (b-m) Rows: PRISM, IF (targeting A β peptides), and lipid (1741 cm^{-1}) images, respectively. Columns: representative WT, diffuse plaque, compact plaque, cored plaque, respectively. Dashed circles: colocalized plaque boundaries. For column 4, the inner circles and outer circles indicate the core and halo, respectively. (n) Boxplot of β -sheet intensity derived from WT and three types of amyloid plaques. (o) Boxplot of the corresponding lipid intensity. The boxes range between the first and third quartiles. Middle bars: median value. Whiskers: max and min values. Outliers are marked by crosses. n.s., not significant; *, $P < 0.05$; **, $P < 0.01$; ***, $P < 0.001$; ****, $P < 0.0001$. (p) Scatterplot of lipid content against β -sheet in amyloid plaques.

with the accumulation of β -sheet (Fig. 2(p)). Notably, the most significant reduction in the lipid level was observed between diffuse and compact plaques, indicating that lipid loss was most pronounced during the transition from diffuse to compact plaques.

2.3. Spatial heterogeneity of plaque-associated lipid across brain regions

Leveraging the submicron spatial resolution by MIP spectroscopy, the molecular composition of amyloid plaques was studied by acquiring *in situ* IR spectra at sub-plaque resolution. Two distinct types of plaque-lipid interactions were identified: the lipid content in lipid-dissociated plaques decreased as β -sheet-rich structures emerged (Fig. 3(a, c), while the lipid content in

lipid-stabilized plaques remained constant (Fig. 3(b), d). These results indicate that plaques can be further classified based on their molecular compositions beyond the previously reported morphological classification.

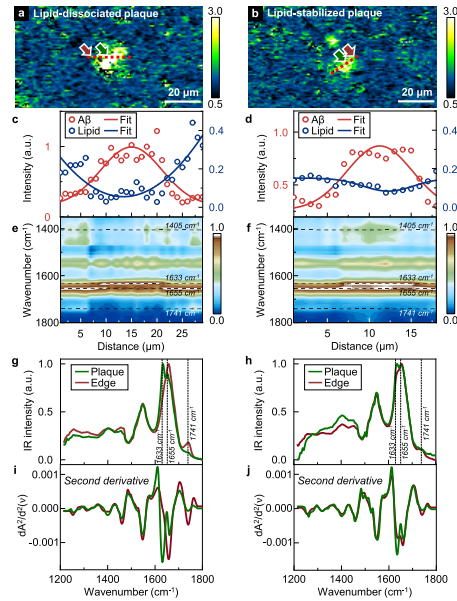


Fig. 3. MIP spectra identifies two plaque subtypes related to lipid. (a, b) PRISM image of a lipid-dissociated plaque and a lipid-stabilized plaque, respectively. (c, d) Intensity profiles and Gauss fitting of the PRISM signal and the 1741cm^{-1} lipid intensity along the dashed lines in (a) and (b), respectively. (e, f) Spectral contour of the IR spectra along the dashed lines in (a) and (b), respectively. (g-j) MIP and second derivative spectra at the body and edge of the lipid-dissociated plaque and the lipid-stabilized plaque indicated by arrows of the same color in (a) and (b), respectively.

To characterize different plaques, spatial-spectral profiling using 1633cm^{-1} and 1741cm^{-1} was performed to visualize the distribution of amyloid plaque and lipid (Fig. 3(e), f). Notably, a fragmented structure at 1405cm^{-1} was observed in lipid-dissociated plaques, whereas a single, stabilized structure was found in lipid-stabilized plaques. This observation may be attributed to changes in carboxyl stretching [53] and myelin [54,55]. Spectral analysis on more than 100 plaques showed a consistent IR spectral profile across three different brain slices obtained from two mice (Fig. 3(g), (h)). Specifically, a red shift of about 20cm^{-1} in the amide I region at the center of the plaques compared to the tissue at the edge was observed, indicating β -sheet accumulation at the center. Importantly, the second derivative spectra (Fig. 3(i), j) of plaque body and edge showed a higher proportion of β structure relative to α structure in lipid-dissociated plaque, indicating more mature plaque formation. These results suggest a potential regulatory mechanism of plaque maturation through plaque-lipid interactions.

To investigate whether different plaque-lipid interactions are enriched in specific brain regions, we measured the contents and projected the two types of plaques onto the entire brain slice (Fig. 4(a)), followed by a statistical analysis of the spatial lipid distributions (Fig. 4(b)). Although lipid-dissociated and lipid-stabilized plaques are found in all major brain regions, we found a particular enrichment of lipid-dissociated plaques with much-lowered occurrence of lipid-stabilized plaques in the hippocampus (Fig. 4(b) and (S6)). This suggests that a specific plaque-lipid interaction may exist in the hippocampus region, which echoes recent findings on the unique role of lipid in the hippocampal pathogenesis of AD, where APOE4 is a major genetic

risk factor for AD [56]. Meanwhile, lipid-stabilized plaques are found mostly in the cortical, cerebral nuclei, and thalamus, which are related to sensory and motor functions.

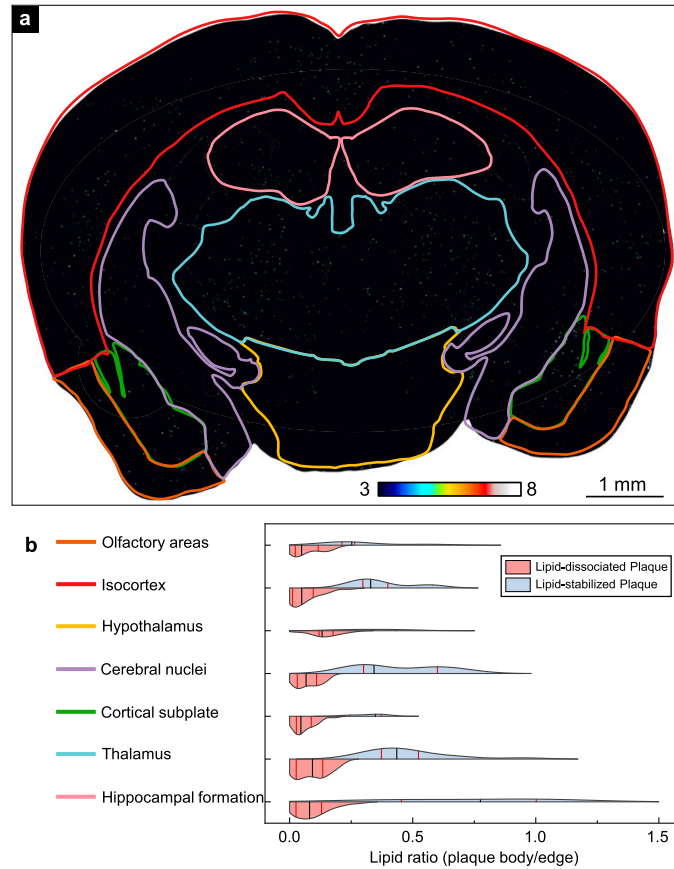


Fig. 4. Statistical analysis of lipid-based subtypes across different brain regions. (a) Plaque distribution (dots) and contours of basic brain regions (line). To prevent zoom distortion, the whole brain map is sharpened. The feature ROIs of 7 basic brain regions were selected to show more details. Scale bars: 50 μm . (b) Split violin diagram of lipid ratio indicating the content distributions of lipid-dissociated plaque (inferior violin) and lipid-stabilized plaque (superior violin) in each brain region as indicated in (a). The Y axis represents the Kernel density estimation of the data. Black vertical bars: median value. Pairs of red vertical bars: the first and third quartiles, respectively.

2.4. Visualization of Tau hyperphosphorylation

We investigate the other crucial pathological feature, NFT, composed of pTau aggregations. By PRISM imaging of β -sheet in the hippocampus, the site for the initial spread of Tau pathology in the brain, an enrichment of β -sheet structure was observed in the granule cell layer in a 6-month-old P301S mouse (Fig. S7a). Notably, distinct from amyloid plaques, a noticeable increase in the 1694 cm^{-1} peak is also observed, which is attributed to the anti-parallel β -sheet (Fig. S7b). Using PRISM imaging of this anti-parallel β -sheet motif at 1694 cm^{-1} , Tau-specific imaging was performed (Fig. 5(a), b), which showed filament-like structures not observable by single wavenumber imaging (Fig. 5(c)). Comprehensive spectral analysis in the fingerprint region from 10 spectra obtained from these filament-like aggregates further showed an elevation of

the phosphate band ($1050\text{--}1150\text{ cm}^{-1}$) compared to adjacent non-pathological areas (Fig. 5(d)), further suggesting phosphorylated form of Tau.

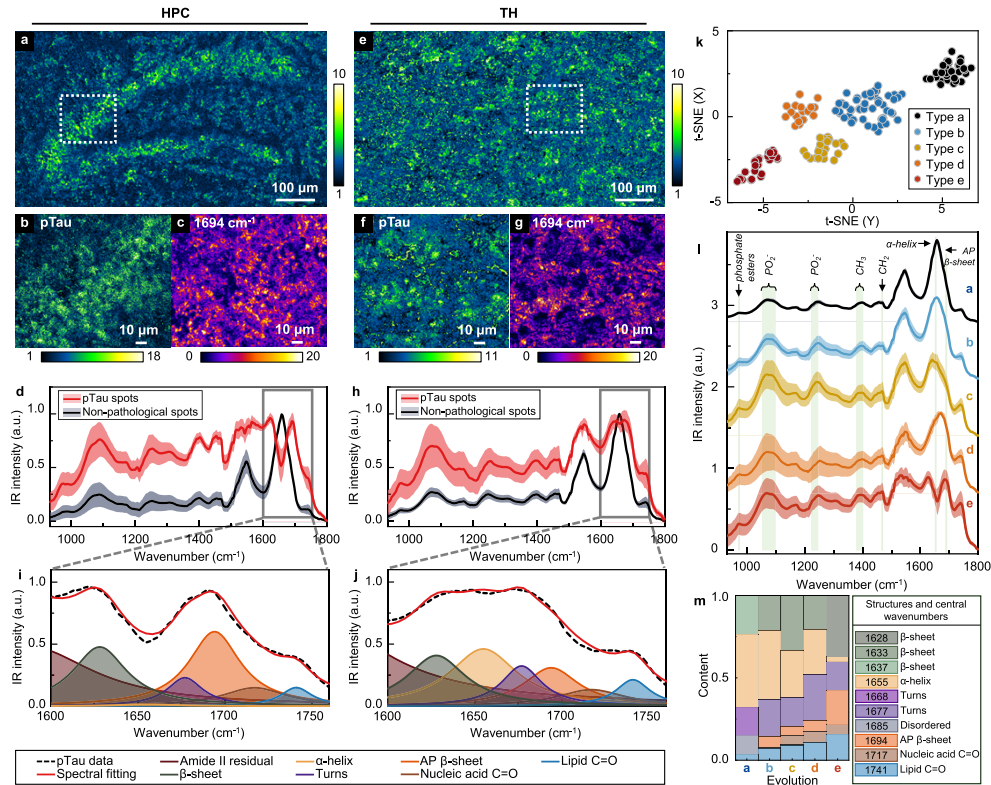


Fig. 5. Visualization of phosphorylated Tau protein. (a) PRISM image of the hippocampus (HPC). (b) Enlarged image of the granule cell layer (dashed box in a). (c) Single wavenumber images of (b) at 1694 cm^{-1} . (d) Spectra of pTau (red) and non-pathological spots (blue). Error bands (shaded area) are standard deviation of 10 different pathological tangles or non-pathological pixels. (e-h) Results for thalamus with the same notes as in (a-d) of the thalamus (TH). (i-j) Quantification of protein and lipid bands of pTau in (d) and (h), respectively. (k) t-SNE map for the distribution of 147 MIP spectra from the thalamus (type a-e). (l) Spectra extracted from each type in (k). Error bands (shaded area) are standard deviation of 10 spectra from 10 different pathological tangles. (m) Percentile stacked histograms of each type of structures quantified in (l). AP β -sheet: anti-parallel β -sheet.

Similarly, PRISM imaging of the anti-parallel β -sheet in the thalamus showed filament-like aggregates (Fig. 5(e-h)). However, the spectral profile of these pTau-aggregates shows distinct features in the amide I and lipid bands ($1599\text{--}1760\text{ cm}^{-1}$). To quantify these differences, we performed deconvolution on pTau and non-aggregated spectra within the hippocampus and the thalamus (Fig. 5(i, j) and S8). An increase in the lipid content in pTau compared to the non-pathological areas indicates a possible relationship between the phosphorylation process and lipid [15]. While non-pathological areas maintained a consistent α -dominance protein conformation (Fig. S8b, d, blue shades), the statistical analysis of the pathological areas in these two brain regions showed the absence of α -helix only in the hippocampus region, which could be attributed to the more advanced pTau pathology in the hippocampus compared thalamus.

Different from amyloid plaque, the pTau spectral profile exhibits much higher diversity. To quantify the intrinsic spectral differences in these structures, we utilized t-distributed stochastic

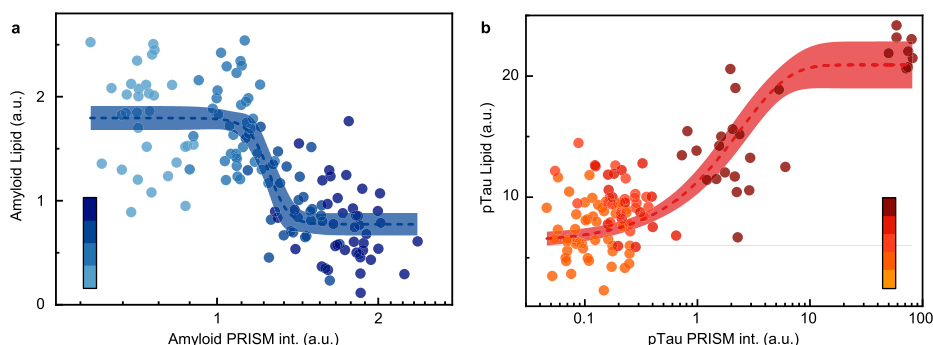


Fig. 6. Lipid-amyloid and lipid-pTau correlations. Predictive projections (dashed lines) and 95% confidence intervals (shades) of lipid in pathological conditions against amyloid deposition (a) and Tau phosphorylation (b). The average PRISM intensity of WT and three different forms of amyloid plaques in Fig. 2 is used and represented with blue color coding in (a). PRISM intensity of pTau from Fig. 5 is used and shown by the color bar in (b). The horizontal scales are logarithmic.

neighbor embedding (t-SNE), a multivariate dimension reduction approach, for analysis (Fig. 5(k)). As a result, five clusters with distinctive spectral characteristics are obtained (representative spectra shown in Fig. 5(l)), which may be attributed to different conformations or packing density [30] of tau filaments. Specifically, the increase in the stretching mode of phosphate esters (971 cm^{-1}) and the broadening and enhancement of the phosphate bands ($1050\text{--}1150\text{ cm}^{-1}$ and $1221\text{--}1250\text{ cm}^{-1}$) indicate an elevated degree of protein phosphorylation [57–59], which correlates with the replacement of α structure with β structure, suggesting protein conformational changes concurrently with Tau phosphorylation. On the other hand, pTau exhibits an increase in the symmetric CH_3 bending modes ($1380\text{--}1405\text{ cm}^{-1}$) and CH_2 bending vibration (1470 cm^{-1}), which is attributed to the alteration in the conformational ratio of the protein and the accumulation of lipid [60].

To explore structural diversity, we quantified protein related structures in the amide I band using spectral fitting (Fig. 5(m), (S9)). From stage a (non-pathological) to stage b, a broadening of the amide I band and an appearance of anti-parallel β -sheet indicating initial protein structure shifts. Stage c exhibited a preference for accumulating β -sheet structures, while stage d shows a pronounced increase in anti-parallel β -sheet formation. Throughout these stages, β -structure content steadily increases, eventually replacing α -helix content by stage e. Additionally, lipid gradually increased, while turn structures decreased. Notably, the central wavenumbers of key protein structures, such as β -sheets and turns, consistently shifted away from the α -helix structure from stage a to stage e. These shifts, driven by changes in intermolecular interactions, suggest a dynamic structural composition in abnormal protein structures [61], consistent with *in vitro* NFT progression studies [62]. Furthermore, our results provide direct visualization evidence of NFT structural dynamics, enabling *in situ* determination of disease development stages. These findings reveal heterogeneity in pTau structures within the brain tissue microenvironment, offering valuable insights for pTau aggregate subtyping.

2.5. Revealing lipid and abnormal protein progression

By tracking lipid components with protein structures at various plaque types, the lipid profile with pathological progression is depicted (Fig. 6), providing evidence of lipid involvement in protein conformational progression. For $\text{A}\beta$, lipid content decreases in later stages of progression, with a rapid decline observed during the intermediate phase (Fig. 6(a)). In contrast, for pTau, lipid start to accumulate at an increased rate as phosphorylation progresses (Fig. 6(b)). The lipid

contents in both cases reach a plateau at the late stages of aggregations. These findings suggest a possibility of a new type of lipid metabolic regulation based on the secondary structures of protein in aggregates. This finding is consistent with a recent study by Haney et al. showing plaque's role in the regulation of lipid metabolism in AD [18]. It would be interesting to investigate in the future whether the content of secondary structures would alter lipid accumulation and the corresponding disease progression.

3. Discussion and conclusion

It is worthwhile to contrast our study with existing techniques for the analysis of protein abnormalities. For instance, electron microscopy, immunofluorescence imaging, Raman, AFM-IR, and mass spectrometry imaging are noteworthy modalities used to target protein structure. While electron microscopy is a valuable tool with superior resolution for studying structures of purified proteins, it has difficulties identifying specific amyloid or tau proteins in a brain tissue slice with a rather limited field of view. To identify specific protein aggregations, immunological staining methods are widely used techniques that exhibit a high degree of specificity in displaying the spatial distribution, which is relatively fast in imaging speed except the lengthy staining process. Meanwhile, mass spectrometry imaging provides more accurate molecular information with large field of view, yet limited by a substantially larger sampling area compared to optical microscopy. Alternatively, Raman or AFM-IR imaging could potentially identify protein secondary structures from amide bands, yet is limited by imaging speed. Nonetheless, stimulated Raman imaging offers fast imaging speed, yet its signal in the fingerprint region is significantly weaker than that in high-wavenumber C-H stretching region. Collectively, PRISM offers a nascent solution to the above challenge with high sensitivity in secondary structures, high resolution, large field of view, non-destructive imaging capability.

Ratio imaging, a commonly employed approach, has been used to characterize neuronal amyloid aggregates by MIP [41]. Nevertheless, direct ratio imaging, heavily reliant on image-provided information, may obscure target structures in highly heterogeneous tissues. The emerging fluorescence-guided MIP micro-spectroscopic technique alleviates this problem, offering avenues for targeting specific molecules [43] and achieving depth-resolved protein visualization in fixed cells seeded with Tau fibrils [42]. While these approaches effectively enable spectroscopic detection and 3D imaging of known protein structures, the guidance of fluorescence limits the exploration of unknown protein misfolding events, as the evolution of diseases like AD involves complex processes with multiple types of protein misfolding. Thus, label-free imaging capability of PRISM provides an effective approach for quantitative chemical imaging.

In conclusion, we developed a molecular spectroscopic imaging approach to quantify protein secondary structures and lipid content in AD, revealing spatial heterogeneity of protein-lipid interactions in unstained mouse brain tissues at submicron resolution. With the rich content from spectroscopy, we observed pathological distribution of A β and pTau and their respective interactions with lipids across brain regions, offering new opportunities in advancing our understanding of neurodegenerative disease mechanisms.

4. Methods

4.1. Study design

5xFAD and P301S mouse models were used in this study. Specifically, for Transgenic 5xFAD mouse model, all animal maintenance and experimental procedures were conducted according to the Westlake University Animal Care Guidelines, and all animal studies were approved by the Institutional Animal Care and Use Committee (IACUC, permit number: 19-044-kp) of Westlake University, Hangzhou, China. Mice were maintained at strict barrier facilities with macroenvironmental temperature and humidity ranges of 20-26 °C and 40-70%, respectively.

Food and water were provided ad libitum. Mouse rooms had a 12 h light/12 h dark cycle. The housing conditions were closely monitored and controlled. Two male 5xFAD adult mice (9 months & 11 months) and one C57BL6 adult male mouse (12 months) were used in these studies. The 5xFAD mice were acquired from the colony currently breeding in Piatkevich lab, Westlake University. Animals were housed under a 12/12 cycle and standardized breeding condition in the Laboratory Animal Research Center of Westlake University. Genotyping of 5xFAD mice was done on the toe-extracted DNA using standard polymerase chain reaction and gel electrophoresis (primers used for transgene detection: Com_Forward: ACC CCC ATG TCA GAG TTC CT; Mut_Reverse: CGG GCC TCT TCG CTA TTA C; Wt_Reverse: TAT ACA ACC TTG GGG GAT GG). For P301S mouse model, mice were kept in cages with a 12 h light/12 h dark cycle. Food and water were available ad libitum. In this experiment, the mouse selected was sacrificed at 6 months of age.

4.2. Preparation of A β 42 peptides

Lyophilized synthetic human 1-42 peptides were purchased from Beyotime Biotechnology (P9001-5 mg). Amyloid peptide stock solution was reconstituted with distilled water and aliquoted to store at -20°C until use. Peptide solution were further diluted in phosphate-buffered saline (PBS) and coated on CaF_2 slides for MIP scanning.

4.3. Biological samples

Frozen 5xFAD brain slice preparation: Animals were deeply anesthetized with 1% sodium pentobarbital (50 mg kg^{-1}) through intraperitoneal injection. After confirming the deep anesthetization, animals were transcardially perfused with 1x PBS and fixed with 4% formaldehyde (EMS, 15714). Brains of perfused animals were carefully dissected and further fixed in 4% formaldehyde for 12 hours at 4°C . Cryoprotection in 30% sucrose solution for 48 hours was performed before embedding in OCT and freezing at -20°C . Frozen samples were cryosectioned into 10-micrometer intervals using a Leica CM1950 cryostat (FCCF-VCM) and the slices containing the hindbrain region with similar hippocampus structures were attached to sticky surfaced microscope slides (CITOTEST, REF.10127105P-G) to be stored at -20°C . **Frozen P301s brain slice preparation:** Fixed mouse brain were dehydrated and embedded in OCT before frozen to -20°C . Frozen samples were cryosectioned into 30-micrometer intervals, placed in cryopreservation solution and frozen to -20°C . Before performing imaging, samples were washed 4 times with 1x PBS and pasted onto slides and stored at -20°C .

4.4. Immunofluorescence staining and imaging

Immunofluorescence staining was performed after PRISM imaging. Brain slices were allowed 20 minutes at room temperature (RT) after being taken out from -20°C . Brain slices were rehydrated with 1x PBS for 10 minutes before staining. The slices were blocked with blocking buffer (5% BSA and 0.3% TritonX-100 in PBS) for 2 hours at RT, then incubated with primary antibody (1:500, A β D54D2 XP, #8243 CST) in a humid chamber for 18 hours at 4°C . Afterward, the slices were washed three times, 5 minutes each in PBS, followed by incubation with secondary antibody (1:1200, Goat anti-Rabbit IgG Alexa Fluor 647, ab150083) for 3.5 hours at RT. The slices were mounted with ProLongTM Gold antifade reagent (INVITROGEN, REF P36930) and covered with coverslips. Immunofluorescent images of stained slices were acquired using a Nikon Eclipse Ti2 fluorescence microscope.

4.5. MIP imaging

The imaging platform was modified based on a configurations described previously [31] from a commercial microscope (mIRage, Photothermal Spectroscopy Corp. CA). A nanosecond pulsed quantum cascade laser was used as a pump beam, and a continuous wave laser (Cobolt, 532 nm,

300 mW) was used as a probe beam. Two beams were spatially overlapped through a dichromatic mirror and transmitted to a reflecting objective lens (PIKE, 40X, 0.78 N.A.). The sample was scanned by a sample displacement table (MLS203, Thorlabs), from which the reflected probe beam from the sample is then transmitted to the photodiode. The collected signal passes through a lock-in amplifier (Zurich, MFLI) and into the computer. The spatial resolution of our system is 387 nm horizontally and 268 nm vertically, with a spectral resolution of about 2 cm^{-1} . The infrared laser powers at the sample used for BSA and A β solutions were about 3.6 mW and 1.6 mW, respectively. The probe power was about 22 mW. For the whole brain slice imaging and spectra of the 5xFAD model, the infrared laser and probe beam powers at the sample were about 0.8 mW and 6 mW, respectively. The images were scanned with a pixel size of $0.8\text{ }\mu\text{m}$, and a pixel dwell time of 2 ms and 1 ms for WT and AD brain slices, respectively. For the imaging and spectra of the P301S model, the infrared laser and probe beam powers at the sample were about 1.6 mW and 11.2 mW, respectively. The pixel size of the images at $0.8\text{ mm} \times 0.45\text{ mm}$ is $0.3\text{ }\mu\text{m}$ and the dwell time is 1.25 ms. The pixel size of the images at $0.14\text{ mm} \times 0.12\text{ mm}$ is $0.1\text{ }\mu\text{m}$ and the dwell time is 3.4 ms. The sweep speed was 100 cm^{-1} per second and averaged 5 times for all spectra. The total acquisition time for a single image of the whole AD brain slice is about 21.8 h.

For 5xFAD model, MIP calculation was performed on the individual images and then 50 images of about $1.8\text{ mm} \times 0.6\text{ mm}$ each in size were stitched according to the recorded motorized stage positions, where the overlapped area was averaged (Python 3.9.13). The whole-brain MIP map was denoised (Python and ImageJ), and pseudo-colored by ImageJ. Holes caused by the presence of air bubbles in the whole-brain map were masked and removed. The MIP spectra were Savitzky-Golay smoothed (5 pts) and then normalized. Plaque distribution map was realized with the help of threshold. For P301S mouse model: MIP calculation was performed on the individual images, then denoised (Python and ImageJ), and pseudo-colored by ImageJ. The spectra were Savitzky-Golay smoothed (5 pts) and normalized.

4.6. Spectral deconvolution

We note that the MIP spectral profile is proportional to the absorbed energy from IR light, in contrast to the logarithmic scale commonly used in FTIR spectroscopy, resulting in less error in fitting using Lorentzian than Gaussian or Voigt functions. Previous studies have demonstrated the reliability of Lorentz deconvolution in protein analysis [42,63]. Here, for protein secondary structure and lipid analysis, we chose $1600\text{--}1750\text{ cm}^{-1}$ window for baseline correction and deconvolution of the spectra. The analysis was performed by the peak analysis application module in Origin 2018.

4.7. MIP image analysis by PRISM

Conventional analysis directly divides two images at respective peak positions. Here, by dividing the 1633 cm^{-1} image by the 1655 cm^{-1} image, distinguishable signals can be observed from the amyloid plaques (Fig. S2b, f). To further enhance the contrast of the specific plaque features, we noticed a background signal at 1633 cm^{-1} , which comes from the α structure content as in WT brain tissue (peak centered at 1655 cm^{-1}). Similarly, a non-negligible signal at 1655 cm^{-1} comes from the β structure contribution. To remove these contributions, two factors are needed: $\alpha(1633)/\alpha(1655)$ and $\beta(1655)/\beta(1633)$, where $\alpha(1633)$ refers to the deconvoluted α structure intensity at 1633 cm^{-1} . The image at 1655 cm^{-1} , i.e., $I(1655)$, is then multiplied by $\alpha(1633)/\alpha(1655)$ and subtracted from $I(1633)$ and vice versa to generate a PRISM image. As a result, a more than 4-fold improvement on amyloid contrast is found (Fig. S2).

4.8. Statistics and reproducibility

For statistical analysis on three stages plaques, the mean values of the selected areas (e.g. plaques) were used as the signal intensity, the regions in WT brain slices with similar sample numbers and

area sizes were randomly selected as control. For the analysis of lipid-dissociated plaque and lipid-stabilized plaque, we made violin plots in different brain regions after analyzing the ratio of lipid signal intensity in the same area region of the plaques and their periphery.

4.9. *t*-SNE evaluates complicated pTau spectra

By extracting both linear and non-linear features from the spectra, it reduces spectra containing information about various biological molecules, from a higher to a lower dimension. We used a perplexity of preserve global structure, an exaggeration of 1 and PCA components of 5 (explained variance of 99%) as parameters. The analysis was performed in the open source data mining software Orange.

Funding. National Natural Science Foundation of China (12074339, 32050410293, 32050410298, 32171093, 82372011); The Leading Innovation and Entrepreneurship Team in Zhejiang Province (2020R01001); Fundamental Research Funds for the Central Universities (2023ZFJH01-01, 2024ZFJH01-01); Start-up funding from the Foundation of Westlake University; 2020 BBRF Young Investigator Grant (28961).

Acknowledgments. We would like to express our gratitude to Mariem Salhi and Xiaoting Sun from Westlake University for their help with animal work.

Disclosures. The authors declare no conflicts of interest.

Data availability. All data could be obtained from the authors upon reasonable request.

Supplemental document. See [Supplement 1](#) for supporting content.

References

1. C. Soto, "Unfolding the role of protein misfolding in neurodegenerative diseases," *Nat. Rev. Neurosci.* **4**(1), 49–60 (2003).
2. C. A. Ross and M. A. Poirier, "Protein aggregation and neurodegenerative disease," *Nat. Med.* **10**(S7), S10–S17 (2004).
3. I. Moreno-Gonzalez and C. Soto, "Misfolded protein aggregates: mechanisms, structures and potential for disease transmission," *Semin. Cell Dev. Biol.* **22**(5), 482–487 (2011).
4. F. M. LaFerla and S. Oddo, "Alzheimer's disease: Abeta, tau and synaptic dysfunction," *Trends Mol. Med.* **11**(4), 170–176 (2005).
5. Y. Compta and T. Revesz, "Neuropathological and Biomarker Findings in Parkinson's Disease and Alzheimer's Disease: From Protein Aggregates to Synaptic Dysfunction," *J. Parkinson's Dis.* **11**(1), 107–121 (2021).
6. C. Giacomelli, S. Daniele, and C. Martini, "Potential biomarkers and novel pharmacological targets in protein aggregation-related neurodegenerative diseases," *Biochem. Pharmacol. (Amsterdam, Neth.)* **131**, 1–15 (2017).
7. W. K. Self and D. M. Holtzman, "Emerging diagnostics and therapeutics for Alzheimer disease," *Nat. Med.* **29**(9), 2187–2199 (2023).
8. Y. Zhang, H. Chen, R. Li, *et al.*, "Amyloid β -based therapy for Alzheimer's disease: Challenges, successes and future," *Signal Transduction Targeted Ther.* **8**(1), 248 (2023).
9. D. Ferreira, L.-O. Wahlund, and E. Westman, "The heterogeneity within Alzheimer's disease," *Aging* **10**(11), 3058–3060 (2018).
10. M. Fändrich, M. Schmidt, and N. Grigorieff, "Recent progress in understanding Alzheimer's β -amyloid structures," *Trends Biochem. Sci.* **36**(6), 338–345 (2011).
11. J.-X. Lu, W. Qiang, W.-M. Yau, *et al.*, "Molecular structure of β -amyloid fibrils in Alzheimer's disease brain tissue," *Cell* **154**(6), 1257–1268 (2013).
12. J.-P. Colletier, A. Laganowsky, M. Landau, *et al.*, "Molecular basis for amyloid- β polymorphism," *Proc. Natl. Acad. Sci.* **108**(41), 16938–16943 (2011).
13. J. Liu, I. Costantino, N. Venugopalan, *et al.*, "Amyloid structure exhibits polymorphism on multiple length scales in human brain tissue," *Sci. Rep.* **6**(1), 33079 (2016).
14. A. Alzheimer, "Über eine eigenartige Erkrankung der Hirnrinde," *Allgemeine Zeitschrift für Psychiatrie und Psychisch-gerichtliche Medizin* **64**, 146–148 (1907).
15. Y. Xu, N. E. Propson, S. Du, *et al.*, "Autophagy deficiency modulates microglial lipid homeostasis and aggravates tau pathology and spreading," *Proc. Natl. Acad. Sci. U.S.A.* **118**(27), e2023418118 (2021).
16. M. J. Moulton, S. Barish, I. Ralhan, *et al.*, "Neuronal ROS-induced glial lipid droplet formation is altered by loss of Alzheimer's disease-associated genes," *Proc. Natl. Acad. Sci.* **118**(52), e2112095118 (2021).
17. M. D. Stuchell-Brereton, M. I. Zimmerman, J. J. Miller, *et al.*, "Apolipoprotein E4 has extensive conformational heterogeneity in lipid-free and lipid-bound forms," *Proc. Natl. Acad. Sci.* **120**(7), e2215371120 (2023).
18. M. S. Haney, R. Pálócsics, C. N. Munson, *et al.*, "APOE4/4 is linked to damaging lipid droplets in Alzheimer's disease microglia," *Nature* **628**(8006), 154–161 (2024).

19. B. Lochocki, B. D. Boon, S. R. Verheul, *et al.*, "Multimodal, label-free fluorescence and Raman imaging of amyloid deposits in snap-frozen Alzheimer's disease human brain tissue," *Commun. Biol.* **4**(1), 474 (2021).
20. M. Ji, M. Arbel, L. Zhang, *et al.*, "Label-free imaging of amyloid plaques in Alzheimer's disease with stimulated Raman scattering microscopy," *Sci. Adv.* **4**(11), eaat7715 (2018).
21. R. Cunha, L. Lafeta, E. A. Fonseca, *et al.*, "Nonlinear and vibrational microscopy for label-free characterization of amyloid-beta plaques in Alzheimer's disease model," *Analyst* **146**(9), 2945–2954 (2021).
22. B. Martial, T. Lefèvre, and M. Auger, "Understanding amyloid fibril formation using protein fragments: structural investigations via vibrational spectroscopy and solid-state NMR," *Biophys. Rev.* **10**(4), 1133–1149 (2018).
23. A. Dong, P. Huang, and W. S. Caughey, "Protein secondary structures in water from second-derivative amide I infrared spectra," *Biochemistry* **29**(13), 3303–3308 (1990).
24. Y. Ji, X. Yang, Z. Ji, *et al.*, "DFT-Calculated IR Spectrum Amide I, II, and III Band Contributions of N-Methylacetamide Fine Components," *ACS Omega* **5**(15), 8572–8578 (2020).
25. J. Kong and S. Yu, "Fourier transform infrared spectroscopic analysis of protein secondary structures," *Acta Biochim Biophys Sin (Shanghai)* **39**(8), 549–559 (2007).
26. D. Rohr, B. D. C. Boon, M. Schuler, *et al.*, "Label-free vibrational imaging of different A β plaque types in Alzheimer's disease reveals sequential events in plaque development," *Acta Neuropathol. Commun.* **8**(1), 222 (2020).
27. N. Benseny-Cases, O. Klementieva, M. Cotte, *et al.*, "Microspectroscopy (μ FTIR) reveals co-localization of lipid oxidation and amyloid plaques in human Alzheimer disease brains," *Anal. Chem.* **86**(24), 12047–12054 (2014).
28. M. P. Confer, B. M. Holcombe, A. G. Foes, *et al.*, "Label-Free Infrared Spectroscopic Imaging Reveals Heterogeneity of beta-Sheet Aggregates in Alzheimer's Disease," *J. Phys. Chem. Lett.* **12**(39), 9662–9671 (2021).
29. J. Waeytens, V. Van Hemelryck, A. Deniset-Besseau, *et al.*, "Characterization by nano-infrared spectroscopy of individual aggregated species of amyloid proteins," *Molecules* **25**(12), 2899 (2020).
30. S. Banerjee and A. Ghosh, "Structurally distinct polymorphs of tau aggregates revealed by nanoscale infrared spectroscopy," *J. Phys. Chem. Lett.* **12**(45), 11035–11041 (2021).
31. D. Zhang, C. Li, C. Zhang, *et al.*, "Depth-resolved mid-infrared photothermal imaging of living cells and organisms with submicrometer spatial resolution," *Sci. Adv.* **2**(9), e1600521 (2016).
32. A. P. Fellows, M. T. L. Casford, and P. B. Davies, "Spectral Analysis and Deconvolution of the Amide I Band of Proteins Presenting with High-Frequency Noise and Baseline Shifts," *Appl. Spectrosc.* **74**(5), 597–615 (2020).
33. M. Jackson and H. H. Mantsch, "The use and misuse of FTIR spectroscopy in the determination of protein structure," *Crit. Rev. Biochem. Mol. Biol.* **30**(2), 95–120 (1995).
34. Z. Li, K. Aleshire, M. Kuno, *et al.*, "Super-Resolution Far-Field Infrared Imaging by Photothermal Heterodyne Imaging," *J. Phys. Chem. B* **121**(37), 8838–8846 (2017).
35. J. M. Lim, C. Park, J. S. Park, *et al.*, "Cytoplasmic Protein Imaging with Mid-Infrared Photothermal Microscopy: Cellular Dynamics of Live Neurons and Oligodendrocytes," *J. Phys. Chem. Lett.* **10**(11), 2857–2861 (2019).
36. M. Tamamitsu, K. Toda, H. Shimada, *et al.*, "Label-free biochemical quantitative phase imaging with mid-infrared photothermal effect," *Optica* **7**(4), 359–366 (2020).
37. M. Schnell, S. Mittal, K. Falahkheirkhah, *et al.*, "All-digital histopathology by infrared-optical hybrid microscopy," *Proc. Natl. Acad. Sci. U.S.A.* **117**(7), 3388–3396 (2020).
38. I. M. Pavlovets, K. Aleshire, G. V. Hartland, *et al.*, "Approaches to mid-infrared, super-resolution imaging and spectroscopy," *Phys. Chem. Chem. Phys.* **22**(8), 4313–4325 (2020).
39. R. Mankar, C. C. Gajjala, C. E. Bueso-Ramos, *et al.*, "Polarization Sensitive Photothermal Mid-Infrared Spectroscopic Imaging of Human Bone Marrow Tissue," *Appl. Spectrosc.* **76**(4), 508–518 (2022).
40. N. Gvazava, S. C. Konings, E. Cepeda-Prado, *et al.*, "Label-Free High-Resolution Photothermal Optical Infrared Spectroscopy for Spatiotemporal Chemical Analysis in Fresh, Hydrated Living Tissues and Embryos," *J. Am. Chem. Soc.* **145**, 24796–24808 (2023).
41. O. Klementieva, C. Sandt, I. Martinsson, *et al.*, "Super-resolution infrared imaging of polymorphic amyloid aggregates directly in neurons," *Adv. Sci.* **7**(6), 1903004 (2020).
42. J. Zhao, L. Jiang, A. Matlock, *et al.*, "Mid-infrared chemical imaging of intracellular tau fibrils using fluorescence-guided computational photothermal microscopy," *Light: Sci. Appl.* **12**(1), 147 (2023).
43. C. Prater, Y. Bai, S. C. Konings, *et al.*, "Fluorescently Guided Optical Photothermal Infrared Microspectroscopy for Protein-Specific Bioimaging at Subcellular Level," *J. Med. Chem.* **66**(4), 2542–2549 (2023).
44. B. Ghosh and K. Agarwal, "Viewing life without labels under optical microscopes," *Commun. Biol.* **6**(1), 559 (2023).
45. H. Zong, C. Yurdakul, Y. Bai, *et al.*, "Background-Suppressed High-Throughput Mid-Infrared Photothermal Microscopy via Pupil Engineering," *ACS Photonics* **8**(11), 3323–3336 (2021).
46. Y. Zhang, C. Yurdakul, A. J. Devaux, *et al.*, "Vibrational Spectroscopic Detection of a Single Virus by Mid-Infrared Photothermal Microscopy," *Anal. Chem.* **93**(8), 4100–4107 (2021).
47. A. Sethuraman, G. Vedantham, T. Imoto, *et al.*, "Protein unfolding at interfaces: slow dynamics of alpha-helix to beta-sheet transition," *Proteins: Struct., Funct., Genet.* **56**(4), 669–678 (2004).
48. J. Seo, W. Hoffmann, S. Warnke, *et al.*, "An infrared spectroscopy approach to follow β -sheet formation in peptide amyloid assemblies," *Nat. Chem.* **9**(1), 39–44 (2017).
49. H. Oakley, S. L. Cole, S. Logan, *et al.*, "Intraneuronal β -amyloid aggregates, neurodegeneration, and neuron loss in transgenic mice with five familial Alzheimer's disease mutations: potential factors in amyloid plaque formation," *J. Neurosci.* **26**(40), 10129–10140 (2006).

50. D. J. Hayne, S. Lim, and P. S. Donnelly, "Metal complexes designed to bind to amyloid-beta for the diagnosis and treatment of Alzheimer's disease," *Chem. Soc. Rev.* **43**(19), 6701–6715 (2014).
51. F. Palombo, F. Tamagnini, J. C. G. Jaynes, *et al.*, "Detection of A β plaque-associated astrogliosis in Alzheimer's disease brain by spectroscopic imaging and immunohistochemistry," *Analyst* **143**(4), 850–857 (2018).
52. E. A. Fonseca, L. Lafeta, R. Cunha, *et al.*, "A fingerprint of amyloid plaques in a bitransgenic animal model of Alzheimer's disease obtained by statistical unmixing analysis of hyperspectral Raman data," *Analyst* **144**(23), 7049–7056 (2019).
53. A. Sgarbossa, S. Monti, F. Lenci, *et al.*, "The effects of ferulic acid on beta-amyloid fibrillar structures investigated through experimental and computational techniques," *Biochim. Biophys. Acta, Gen. Subj.* **1830**(4), 2924–2937 (2013).
54. I. Kaya, E. Jennische, S. Lange, *et al.*, "Brain region-specific amyloid plaque-associated myelin lipid loss, APOE deposition and disruption of the myelin sheath in familial Alzheimer's disease mice," *J. Neurochem.* **154**(1), 84–98 (2020).
55. S. Qiu, J. P. Palavicini, J. Wang, *et al.*, "Adult-onset CNS myelin sulfatide deficiency is sufficient to cause Alzheimer's disease-like neuroinflammation and cognitive impairment," *Mol. Neurodegener.* **16**(1), 64 (2021).
56. X. Zhang, R. Gao, L. Yang, *et al.*, "Astrocytic functions and lipid metabolism: Correlations and therapeutic targets in Alzheimer's disease and glioblastoma," *Clin. Transl. Discovery* **4**(2), e287 (2024).
57. B. R. Wood, M. A. Quinn, F. R. Burden, *et al.*, "An investigation into FTIR spectroscopy as a biodiagnostic tool for cervical cancer," *Biospectroscopy* **2**(3), 143–153 (1998).
58. S. Yoshida, M. Miyazaki, K. Sakai, *et al.*, "Fourier transform infrared spectroscopic analysis of rat brain microsomal membranes modified by dietary fatty acids: possible correlation with altered learning behavior," *Biospectroscopy* **3**(4), 281–290 (1997).
59. T. Richter, G. Steiner, M. H. Abu-Id, *et al.*, "Identification of tumor tissue by FTIR spectroscopy in combination with positron emission tomography," *Vib. Spectrosc.* **28**(1), 103–110 (2002).
60. H. Wang, H.-C. Wang, and Y.-J. Huang, "Microscopic FTIR studies of lung cancer cells in pleural fluid," *Sci. Total Environ.* **204**(3), 283–287 (1997).
61. C. M. Moloney, V. J. Lowe, and M. E. Murray, "Visualization of neurofibrillary tangle maturity in Alzheimer's disease: A clinicopathologic perspective for biomarker research," *Alzheimer's Dementia* **17**(9), 1554–1574 (2021).
62. L. Pinzi, N. Bisi, C. Sorbi, *et al.*, "Insights into the structural conformations of the tau protein in different aggregation status," *Molecules* **28**(11), 4544 (2023).
63. H. Yang, S. Yang, J. Kong, *et al.*, "Obtaining information about protein secondary structures in aqueous solution using Fourier transform IR spectroscopy," *Nat. Protoc.* **10**(3), 382–396 (2015).